Supporting Online Material for

Kepler-9: A System of Multiple Planets Transiting a Sun-Like Star, Confirmed by Timing Variations

Matthew J. Holman,* Daniel C. Fabrycky, Darin Ragozzine, Eric B. Ford, Jason H. Steffen, William F. Welsh, Jack J. Lissauer, David W. Latham, Geoffrey W. Marcy, Lucianne M. Walkowicz, Natalie M. Batalha, Jon M. Jenkins, Jason F. Rowe, William D. Cochran, Francois Fressin, Guillermo Torres, Lars A. Buchhave, Dimitar D. Sasselov, William J. Borucki, David G. Koch, Gibor Basri, Timothy M. Brown, Douglas A. Caldwell, David Charbonneau, Edward W. Dunham, Thomas N. Gautier III, John C. Geary, Ronald L. Gilliland, Michael R. Haas, Steve B. Howell, David R. Ciardi, Michael Endl, Debra Fischer, Gábor Fürész, Joel D. Hartman, Howard Isaacson, John A. Johnson, Phillip J. MacQueen, Althea V. Moorhead, Robert C. Morehead, Jerome A. Orosz

*To whom correspondence should be addressed. E-mail: mholman@cfa.harvard.edu

Published 26 August 2010 on *Science* Express
DOI: 10.1126/science.1195778

This PDF file includes:

Supporting Online Material

Stellar Properties from the Kepler Input Catalog The Kepler Input Catalog (KIC) used ground-based multi-band photometry to assign an effective temperature, surface gravity, and metallicity of $T_{\rm eff} = 5722$ K, $\log g = 4.78$ (cgs), and [Fe/H]$= 0.17$ to Kepler-9 (KIC 3323887, 2MASS 19021775+3824032, $\alpha = 19^{\rm h}02^{\rm m}17^{\rm s}.76$, $\delta = +38^\circ24'03''.2$, J2000, KIC $r = 13.731$, $K_p = 13.308$, $g - r = 0.516$, $J - K = 0.374$). Stellar gravities in this part of the H-R diagram are notoriously difficult to determine from photometry alone, and the KIC value for the surface gravity seems high for a star that otherwise appears to be very similar to the Sun. The KIC uses the surface gravity to estimate the stellar radius, so consequently this suggests that the KIC value of $R_\star = 0.677\ R_\odot$ is too small. The spectroscopic observations reported in the next section support this conclusion, as well as the analysis of the combination of photometry and radial velocity.

Reconnaissance Spectroscopy Reconnaissance spectra serve to determine basic stellar parameters of the host star, as well as to search for evidence of a stellar companion or a nearby background eclipsing binary system that might be causing the apparent transit signal in the light curve.

The first reconnaissance spectrum was obtained with the Tull Coudé Spectrograph of the McDonald Observatory 2.7m Harlan J. Smith Telescope on 25 May 2010UT. This spectrum was cross-correlated against a library grid of synthetic spectra to find the match with the highest correlation coefficient. The best match was a spectrum with effective temperature $T_{\rm eff} = 5750$ K, $\log g = 4.5$, [Fe/H] $= 0.0$, and $v \sin i = 0\ {\rm km\,s^{-1}}$. The $T_{\rm eff}$ spacing in the library of synthetic spectra is 250 K . The [Fe/H] spacing is 0.5 dex. The rotational velocity spacing is nonuniform: 0, 1, 2, 4, 6, 8, 10, 12, 16 20, 25, 30, 35, 40, 50, 60, 70, 80, 90, 100, 120, 140, 160, 180, 200 ${\rm km\,s^{-1}}$, implying uncertainties no smaller than half the spacing. The cross-correlation peak

was very narrow, without any nearby peaks, indicating Kepler-9 is a slowly rotating solar-type star. There was no obvious evidence of a composite spectrum.

Subsequently, we obtained a high resolution spectrum of higher SNR with the Keck-HIRES spectrometer. A 3 minute exposure yielded a spectrum with SNR per pixel of 25 (4% fractional errors in each pixel of size 1.3 km s^{-1}). We carried out a standard LTE spectral synthesis using SME to obtain the following stellar parameters: $T_{\rm eff} = 5777 \pm 61$ K, $\log g = 4.49 \pm 0.09$, $v \sin i = 1.9 \pm 0.5$ km s^{-1}, and [Fe/H] $= +0.12 \pm 0.04$. These stellar parameters agree, within errors, with those obtained from the McDonald spectrum. Kepler-9 is apparently a G2 main sequence star with slightly higher than solar metallicity. Our spectra of the Ca II H&K line show an emission reversal indicative of a slightly more active chromosphere than that of the Sun, which is also consistent with the fractional coverage of starspots and the faster rotation rate.

Kepler Photometry Kepler-9 was on the original Kepler Planetary Target List (*1*), but it was not observed during commissioning (Q0) due to its faintness. It has been observed during each quarter of Kepler observations, nearly continuously since BJD 2454964.5122643. Kepler observations are divided into quarters, between which the spacecraft performs a roll in order to realign its solar arrays. The observations discussed in this paper cover Quarters 1-3, during which Kepler-9 was observed with a $\sim$93% duty cycle over nearly 218 days. Occasional dropouts resulted in missing or corrupting two transits of Kepler-9b near 115.7 and 192.7 (BJD-2454900.0), which are not used in our analysis.

The light curve data for Kepler-9 are available electronically from the Multimission Archive at the Space Telescope Science Institute (MAST) web site [1]. Our analysis uses the "raw aperture" photometry obtained from binary FITS tables.

[1] http://archive.stsci.edu/kepler/data_search/search.php

The raw photometry is shown in Fig. 1 of the main text. A detrending algorithm is then used to remove long-term trends and to renormalize the entire light curve so that the out-of-transit flux is set equal to 1. Although various detrending algorithms gave similar results, the data we used was made by applying a 999-minute-long sliding window, wherein a robust cubic polynomial was fit to out-of-transit data, and then used as the normalization factor. The results of this detrending are seen in Fig. 2 of the main text. The data clearly show two periodic signals of planet candidates (which are visible even in the raw data) with slightly different depths, with the deeper transit repeating every $\sim$19 days and the shallower transit repeating every $\sim$39 days. The photometric scatter changes slightly as a function of time, but the typical photometric error in the 30-min long-cadence data shown here is $\sim$210 parts per million (ppm), near the expected value for a star of this brightness.

We have examined the raw light curve for periodicities (due to spots or plage) indicative of the star's rotation. The results depend upon the type of detrending used. However, a rotation period of $\sim$ 16.7 d can be deduced. Such a rotation period is, at first, surprising, as the rotational $v \sin i$ of 1.9 km/s implies (if viewed edge-on) a rotation rate nearly identical to that of the Sun that has a rotational period of 27 days. However, the uncertainty in $v \sin i$ of 0.5 km s^{-1} allows for a possible equatorial velocity of 2.5 km s^{-1} corresponding to a spin period of 16.7 d. In addition, the photometry shows fluctuations on time scale of days that are 5 times greater in amplitude than those seen in the active Sun. Thus a consistent assessment emerges of Kepler-9 as a sun-like star rotating 25% faster than the Sun, with a slightly more active magnetic field and a presumably younger age of 2-4 Gyr (*2*). That the rotation rate is near the orbital period of Kepler-9b is not considered significant as the tidal connection between the star and planet at this distance is very weak.

Radial Velocity Observations We obtained six radial velocity (RV) measurements of Kepler-9 with $\sim$2 $\mathrm{m\,s^{-1}}$ precision using the HIRES echelle spectrometer (*3*) at Keck Observatory using the same Doppler analysis used for two thousand nearby FGKM stars by the California Planet Survey, including use of iodine lines to set both the wavelength scale and the instrumental profile of the spectrometer (*4*). The exposures were 45 minutes, using a slit 0.87×3 arcsec when no Moon was present, and 0.87 x 14 arcsec when the Moon was up, enabling sky subtraction.The resulting spectra have 10,000 photons per pixel (having a size, 1300 $\mathrm{m\,s^{-1}}$). The Doppler analysis of the spectra yielded an internal error (uncertainty in the mean of 400 spectral regions) of 2.5 $\mathrm{m\,s^{-1}}$. For stars of this spectral type an additional RV "jitter" of 2 $\mathrm{m\,s^{-1}}$ is expected (*5*,*6*).

At Kepler magnitude Kp = 13.8 (V=13.9), Kepler-9 is among the faintest stars for which precise Doppler work has been attempted, leading to low signal-to-noise ratios of $\sim$100 per pixel in the Keck HIRES spectra. The deconvolution of the spectrum, as part of the Doppler analysis, is challenged at such noise levels. We attempted two such algorithms, one involving a Jansson deconvolution (*7*) and the other a sum of Gaussians with least-squares fitting, both yielding obvious ringing and enhanced noise in the resulting deconvolved spectrum. We settled on the use of the intrinsic spectrum of the Sun as a better proxy for the intrinsic spectrum of Kepler-9 (*8*). The solar spectrum as the deconvolved template in the Doppler analysis yielded both better fits to the spectrum of Kepler-9 and also smaller internal Doppler errors than the other two deconvolved spectra.

We scheduled the last two observations near JD 2455367 and 2455377, predicted to be a maximum and minimum in velocity, based on the transit ephemeris and dynamical modeling of the Kepler photometry, with the goal of constraining the masses of the two outer planets. The resulting velocities are given in Table S1, and indeed they are well fit by the two-planet Keplerian model, even without dynamical effects included. However, to identify these planets without photometry would have required an order-of-magnitude more RV measurements.

BJD (days)	RV (m/s)	$\sigma_{\rm RV}$ (m/s)
2455342.947836	17.15	2.51
2455344.061419	2.23	2.74
2455351.037415	-7.89	2.36
2455352.011289	-4.61	2.21
2455367.083543	-25.45	2.49
2455376.930532	17.39	2.61

Table S1: Relative Radial-Velocity Measurements of Kepler-9. Radial velocities measured using the NSO solar spectrum as a template.

We caution that with so few RV measurements, it is not possible to directly confirm the hypothesis that the observed stellar motion is due only to Kepler-9b and c. Though the scatter of the residuals from our best-fit two-planet model is relatively low (Figure 1 in the main text), additional contributions to the RV observations from stellar activity, KOI-377.03, additional non-transiting planets, or unmodeled systematic effects cannot be completely ruled out. The main contribution of the RV data is to put tighter limits on the masses of Kepler-9b and c, though the importance of this measurement will diminish as additional transit times are measured (see below).

Bisector Analysis We completed an analysis of the line bisectors of Kepler-9 to look for variations that correlate with the observed transit periods. For this we examined the Keck HIRES spectra, with the results listed in Table S2. Six of the spectra are the 2700 s exposures used for high-precision RV measures; the additional 2700 s exposures is the template spectrum taken without the iodine cell. The other three correspond to 300 s reconnaissance spectra, which work as well for this purpose. We used all the orders from the blue chip, unaffected by the iodine cell. We used a synthetic library spectrum as the template ($T_{\rm eff} = 5750$ K, $\log g = 4.5$, and $v_{rot} = 2 {\rm km\,s^{-1}}$). The bisector variations taken close in time agree well, even with the shorter integration times. The bisectors were measured with cuts at 0.9 and 0.4 of the maximum value

of the peak in the cross-correlation. No significant correlation with the measured transit periods is observed.

Three early Keck HIRES spectra of Kepler-9 show line shape variations of $\sim$100 m/s that remain unexplained. Possible explanations include the use of different slit lengths and the inability to subtract a moonlit sky in two of them. Indeed, simulations of the amount and Doppler shift of moonlight relative to the stellar spectrum show that moonlight contamination could have caused the bisector variations in those early spectra. Nonetheless, no adequate explanation for the bisector variations has emerged, and the subsequent constancy of the line shapes offers a suggestion of some instrumental cause of the earlier line-shape variations.

HJD (days)	phase	line bisector (m/s)	uncertainty (m/s)	exptime (s)
2455342.930269	236.854	85.1	12.0	180
2455342.947779	236.865	75.3	7.7	2700
2455344.061301	237.564	143.5	12.9	2700
2455351.001919	241.923	-27.7	4.6	2700
2455351.037471	241.945	-41.9	6.3	2700
2455352.011541	242.557	-37.6	5.1	2700
2455367.083590	252.021	-53.3	6.3	2700
2455373.075713	255.784	-25.2	8.1	300
2455373.978910	256.351	-46.3	6.0	300
2455376.930303	258.204	-46.7	7.1	2700
2455378.027101	258.893	-25.2	8.2	300

Table S2: Line bisector measurements of Kepler-9. The RMS line bisector value is 67.73 m/s. However, this scatter is due primarily to the large positive values of three early Keck HIRES spectra.

Analysis of Transit Light Curves We analyzed the normalized light curves using a standard transit model with a 4th order non-linear limb darkening model (*9*). Since a transiting planet can move a significant fraction of a stellar radius during 30 minutes (the effective exposure time of Kepler long cadence observations), we numerically integrated over time within each exposure

(*10, 11*). We adopted limb darkening coefficients (see Table S3) that were calculated explicitly for the Kepler bandpass using PHOEBE (*12*) and ATLAS (*13*) models and the observed spectroscopic parameters.

quarter	c1	c2	c3	c4
1	1.0970760	-1.388811856	1.868467888	-0.723973888
2	1.1051112	-1.402470064	1.873991088	-0.725071296
3	1.1041112	-1.401352656	1.873579088	-0.724657264

Table S3: Theoretical non-linear limb darkening parameters for Kepler-9. They change from quarter to quarter because Kepler-9 falls on different CCDs with slightly different color responses; the variations from quarter to quarter do not significantly change the results, but are used for completeness.

First, each transit event was fit individually via Levenberg-Marquardt minimization (*14*), allowing the mid-time of transit (t_c), transit duration (D), planet-star radius ratio (p), and impact parameter (b), the local light curve normalization (n) and a linear slope parameter (s) to vary. The durations and impact parameters were similar for all transits. Two values of the fitted planet-star radius ratio were seen, one for each planet. The approximate periods were based on fitting a quadratic ephemeris ($t_N = t_0 + P \times N + c \times N2$) to the initial fits for transit times of each planet. This supports the originally proposed model of two transiting planets with periods of approximately P_1=19.2 (Kepler-9b) and $P_2 = 38.9$ (Kepler-9c) days, within 3% of an exact 2:1 orbital frequency commensurability.

Second, we constructed a "folded" light curve for each planet candidate, but shifting the data around each transit by the previously fit transit times rather than a linear ephemeris. We again use Levenberg-Marquardt minimization to fit a single transit model to the folded light curve for each planet, allowing D_i, p_i, b_i, n_i and s_i to float, where the subscript i indicates which planet candidate. This light curve was used as a template to measure transit times.

Next, we obtain the final transit times by fitting each transit event individually, allowing the mid-time of transit, local normalization and slope to float, but fixing the transit duration,

planet-star radius ratio, and impact parameter at the values estimated from the previous step. The results are reported in Tables S4 and S5.

Number	T_0 (BJD-2454900.0)	T_1 (BJD-2454900.0)	D	$b/R_\star$
-5	77.24875 ± 0.00059	77.24893 ± 0.00059	0.1571 ± 0.0013	0.650 ± 0.021
-4	96.48240 ± 0.00062	96.48228 ± 0.00064	0.1632 ± 0.0015	0.641 ± 0.021
-2	134.95437 ± 0.00052	134.95445 ± 0.00051	0.1580 ± 0.0012	0.630 ± 0.019
-1	154.19058 ± 0.00052	154.19059 ± 0.00053	0.1597 ± 0.0012	0.679 ± 0.016
0	173.43412 ± 0.00072	173.43485 ± 0.00114	0.1582 ± 0.0025	0.668 ± 0.017
2	211.92589 ± 0.00050	211.92575 ± 0.00050	0.1613 ± 0.0011	0.648 ± 0.017
3	231.17167 ± 0.00048	231.17166 ± 0.00049	0.1592 ± 0.0011	0.672 ± 0.016
4	250.42951 ± 0.00048	250.42940 ± 0.00048	0.1580 ± 0.0011	0.627 ± 0.018
5	269.68103 ± 0.00046	269.68095 ± 0.00048	0.1594 ± 0.0010	0.694 ± 0.014

Table S4: Transit times of Kepler-9b. The times reported in column 2, T_0, correspond to those measured when using values of planet-star radius ratio, transit duration, and scaled impact parameter that are common to all transits of Kepler-9b. In this case, the planet-star radius ratio is $p = 0.07884 \pm 0.00081$, the transit duration is $D = 0.15927 \pm 0.00044$, and the scaled impact parameter is $b/R_\star = 0.654 \pm 0.033$. The times reported in column 3, T_1, along with the transit durations D and scaled impact parameter $b/R_\star$, correspond to the fits for which these values were allowed to vary from transit to transit. In this case, the planet-star radius ratio is fixed at $p = 0.07899$. We recommend adopting measurement uncertainties which are 1.48 times larger than the formal uncertainties reported above, based on the bootstrap analysis described in the text.

Finally, we constructed an updated folded light curve for each planet candidate and refit for the shared parameters (D_i, p_i and b_i) which are reported in Table 1 in the main text. While the formal uncertainties are small, they are very likely underestimated due to uncertainty in the limb darkening coefficients, which are held fixed in our model. Since the nodal angle $\Delta\Omega_{sky}$ cannot be constrained photometrically, the true mutual inclination could be larger than the difference of the two inclinations. Nevertheless, we recognize that the transit light curves are consistent with two planets with a small relative inclination. This is to be expected (if such planetary systems exist), since the probability that two planets both transit a common host star drops significantly as the relative inclination increases beyond 2°, based on the formulae of (*15*).

Number	T_0 (BJD-2454900.0)	T_1 (BJD-2454900.0)	D	$b/R_\star$
-3	69.30577 $\pm$ 0.00070	69.30580 $\pm$ 0.00067	0.1744 $\pm$ 0.0014	0.706 $\pm$ 0.016
-2	108.33086 $\pm$ 0.00061	108.33104 $\pm$ 0.00060	0.1725 $\pm$ 0.0013	0.725 $\pm$ 0.013
-1	147.33560 $\pm$ 0.00058	147.33526 $\pm$ 0.00055	0.1696 $\pm$ 0.0012	0.681 $\pm$ 0.017
0	186.31251 $\pm$ 0.00059	186.31252 $\pm$ 0.00058	0.1757 $\pm$ 0.0013	0.695 $\pm$ 0.015
1	225.26284 $\pm$ 0.00053	225.26267 $\pm$ 0.00054	0.1695 $\pm$ 0.0012	0.737 $\pm$ 0.013
2	264.18168 $\pm$ 0.00055	264.18191 $\pm$ 0.00054	0.1697 $\pm$ 0.0012	0.705 $\pm$ 0.014

Table S5: Transit times of Kepler-9c. As in the previous table, the times reported in column 2, T_0, correspond to those measured when using values of the planet-star radius ratio, transit duration, and scaled impact parameter that are common to all transits of Kepler-9c. In this case, the planet-star radius ratio is $p = 0.07708 \pm 0.00080$, the transit duration is $D = 0.17121 \pm 0.00057$, and the scaled impact parameter is $b/R_\star = 0.715 \pm 0.026$. The times reported in column 3, T_1, along with the transit durations D and scaled impact parameter $b/R_\star$, correspond to the fits for which these values were allowed to vary from transit to transit. In this case, the planet-star radius ratio is fixed at $p = 0.07708$. We recommend adopting measurement uncertainties which are 1.81 times larger than the formal uncertainties reported above, based on the bootstrap analysis described in the text.

Accuracy of Transit Times Our first estimate of uncertainties is based on the covariance matrix evaluated with the best-fit parameters. The χ^2 per degree of freedom of the best fit is $\sim$ 2, hinting that the true uncertainties may be larger than these formal uncertainties.

Next, we questioned whether the light curve normalization could be affecting our transit time measurements. We repeated the analysis using two independent (but related) normalization and smoothing algorithms. We also repeated the analysis with different sizes of the sliding window used for the smoothing. We found that the best-fit transit times differed by significantly less than the formal uncertainty in the transit times. We also measured transit times with alternative limb darkening parameters. Using a quadratic limb-darkening model (*9*) and allowing the coefficients to vary over a range ($\gamma_1 = 0.51 \pm 0.01$, $\gamma_2 = 0.140 \pm 0.005$) consistent with the quoted uncertainties in stellar parameters for Kepler-9 ($\sigma_{T_{\rm eff}}$ = 100K, $\sigma_{\rm [Fe/H]} = 0.1$ and $\sigma_{\log g} = 0.15$) produces variations in transit times that are, at most, 2×10^{-5} days, less than any of the ephemeris uncertainties. Similarly, the choice of model (quadratic versus nonlinear)

proved insignificant for the determination of transit times. While the choice of limb darkening model affected the derived impact parameter, the measured transit times changed by much less than the formal measurement uncertainties.

Finally, we performed a bootstrap-style analysis. We used a template light curve to generate synthetic light curves with an additional transit inserted into the raw light curve (prior to normalization). We chose times randomly, while avoiding times which would result in the smoothed light curve including observations affected by a transit of Kepler-9b and Kepler-9c. The synthetic data were processed with the same detrending algorithm as was applied to the actual data (see SOM Kepler Photometry). Then, we fit the template light curve to each synthetic transit, allowing the midtime of transit, local normalization and slope to varry. Finally, we compared the distribution of the difference between the actual and best-fit transit times for the synthetic transits. The distributions are well described by Gaussians with standard deviations of 78 and 92 seconds for templates corresponding to Kepler-9b and Kepler-9c. These are factors of 1.81 and 1.48 times larger than the median of the formal uncertainties for the transit times of the two planet candidates. For our subsequent analysis we assume that transit times are normally distributed about the true value with standard deviations of the formal uncertainties (reported in Tables S4 and S5) scaled by the above factors. This approach has the advantage that it preserves information about the relative accuracy of measurements of different transits (e.g., one transit of Kepler-9b is missing an observation during ingress).

The presence of spots are an interesting source of non-white noise for transit timings in that the occultation of a spot by the planet can change the transit shape and thereby affect the transit time. To estimate the maximum effect this can have on our timing measurements, we created simulated light curves that include two star spots that approximately match segments of the out-of-transit light curve, and allow Kepler-9b to transit over these spots. The spot's latitude was set to produce the maximum effect in the transit, i.e., the planet was assumed to directly

cross over the spot. Since the observations are in 30-min duration bins, the effect of the spots in the transit light curve is much more subtle than if the upward spike during spot eclipse were well resolved in time. The simulations produced an RMS scatter of 1.4 min in the transit times, with a peak-to-peak variation of $\sim$5 min. Thus even in this worst-case scenario, the presence of the spots on this star cannot induce systematic transit timing variations that are more than a very small fraction of the O-C variations. The spots can induce variations comparable in size to the "chopping" timing variations, but the consistency of the chopping in amplitude and time suggests they are not substantially effected by spots. Furthermore the spot-induced variations are expected to be quasi-random, not alternating, because the spots' lifetimes are only a few weeks, their longitude on the star is random, and the star's spin is not synchronized with the planets' orbits. Finally, since only a small fraction of the star is spotted, it is quite possible that the planet does not transit over any spots in these *Kepler* observations. In summary, the transit timings are robust and the presence of starspots does not substantially contaminate the timing signal.

We analyze KOI-377.03 separately, excluding events which are affected by transits of either Kepler-9b or Kepler-9c. In principle, transit events associated with KOI-377.03 (or other undetected planets) could induce timing variations in Kepler-9b or Kepler-9c. Indeed, the two last transits of Kepler-9b are affected by overlapping transits with KOI-377.03. In practice, the events associated with KOI-377.03 are so shallow that their effect on the transit times measurements for Kepler-9b or Kepler-9c is significantly less than the measurement uncertainties. (For the same reason, mutual events between Kepler-9b and KOI-377.03 (*15*) are too weak to observe). Further, our bootstrap analysis does *not* excludes times associated with KOI-377.03 events. Therefore, the distribution of errors in the transit times fit to the synthetic data includes the effect of KOI-377.03, as well as variability of the target star and any blended objects.

Transit Durations and Shapes The transit duration depends on the stellar radius and the velocity of the planet projected onto the sky at the time of transit. For a planet on a circular orbit, Kepler's law specifies the planet's velocity for a given orbital period and stellar mass. In this case, the transit duration depends on the orbital period, the impact parameter, the stellar density and (for some definitions of transit duration) the size of the planet. In some cases, precise measurement of the transit light curve can provide an estimate of the stellar density (*16–18*). For two planets transiting the same star, the measured ratio of the transit duration to the one third power of the orbital period should be consistent. We calculate $\xi \equiv (D_{in}/D_{out})(P_{out}/P_{in})^{1/3}$, where D is the transit duration and P is the orbital period. We then compare to the distribution of ratios from Monte Carlo simulations (see Fig. S1). The top panels show the probability of transit for each planet individually and both planets, as a function of the relative inclination, assuming that the invariable plane is oriented isotropically. The bottom panels show the distribution of ξ as a function of the relative inclination. For circular orbits (left panels), the median value is slightly greater than unity. The distribution of ξ is somewhat broader for eccentric orbits (right panels). For Kepler-9b and 9c, we measure $\xi_{bc} = 1.18 \pm 0.01$, consistent with expectations for a pair of objects around a common star. The ratio drops to 1.09, if we correct for the best-fit impact parameters, but we caution these are not well constrained with the present data. In either case, ξ_{bc} does not provide evidence for non-coplanarity or non-circular orbits, although the measured ξ_{bc} is consistant with either possibility.

We also test whether the transit duration of KOI 377.03 is consistent with it orbiting the same star. We measure $\xi_{03,b} = 1.16 \pm 0.02$, again consistent with our Monte Carlo simulations.

Even in the restricted case of a planet on a circular orbit, measuring the stellar density is complicated by the sensitivity of the measured impact parameter (or timescale for ingress and egress) on the limb darkening model (*20*). This approximate degeneracy also makes it difficult to constrain the eccentricity and pericenter direction from the transit light curve. In the case of

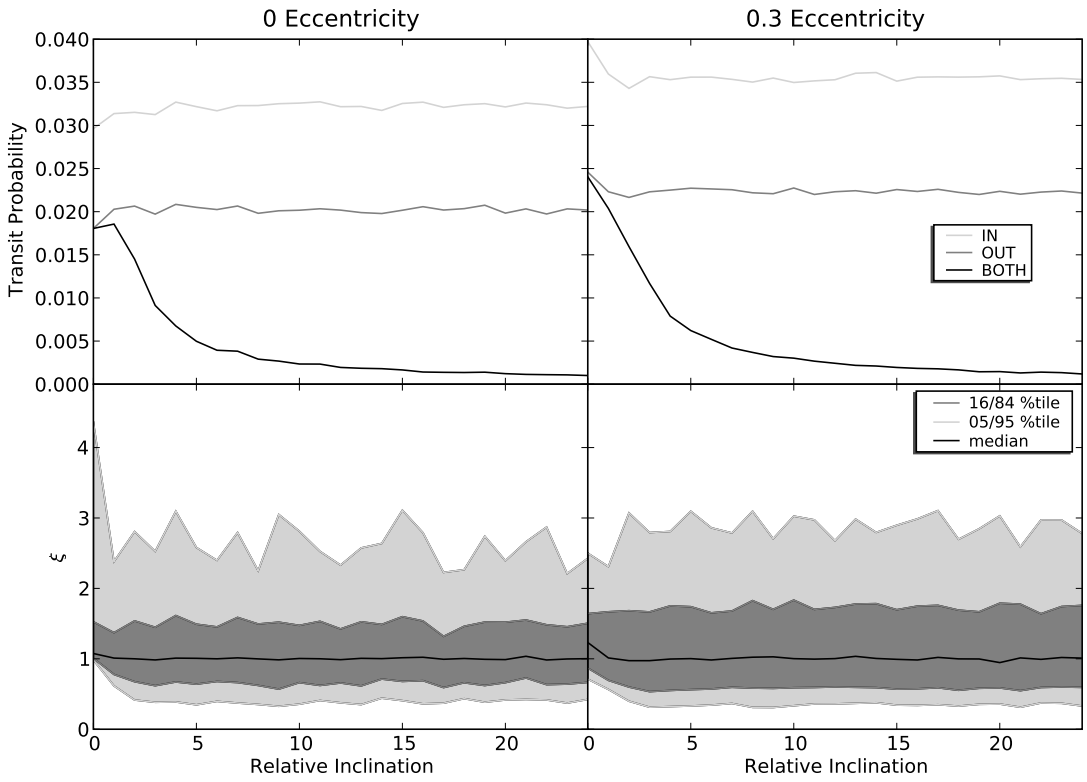

Figure S1: Transit probabilities and ξ distribution for a pair of planets similar to Kepler-9 b & c from Monte Carlo simulation. The top panels show the transit probability for the inner planet (light gray curve), outer planet (medium gray curve) and the combined probability of both transiting (black line) as a function of relative inclination. The left panel is for circular orbits while the right shows the slight enhancement from assigning a moderate eccentricity of 0.3 to each planet. The bottom panels show the distribution of ξ as a function of relative inclination for the 0 and 0.3 eccentricity cases. The black curve corresponds to the median value of ξ, while the dark grey region is bounded by the 16th and 84th percentiles and light grey region by the 5th and 95th percentiles. The x-axis is scaled to relative inclinations of less than ~ 25 to highlight the low relative inclination region. The transit durations used to compute ξ where calculated analytically (*19*) and include the assumed planetary radius of 1 R_{jup} so are computed from 1st to 4th contact, though the results of the simulations are not sensitive to these assumptions.

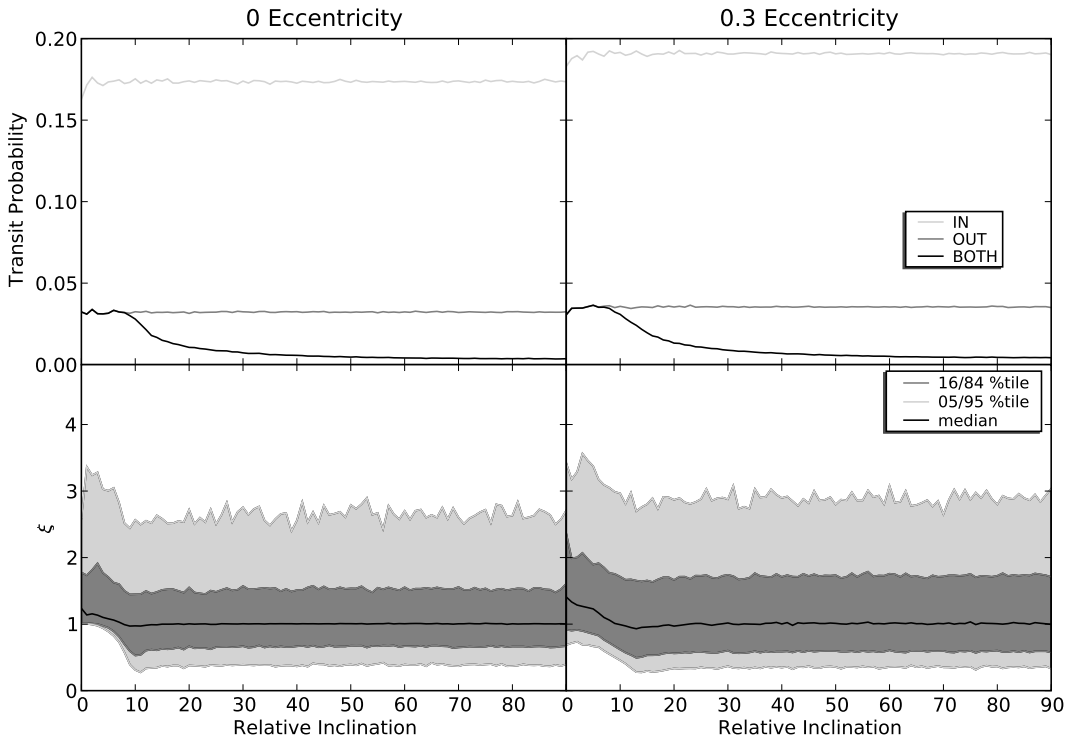

Figure S2: Same as figure S1 except for a pair of planets with orbital periods of 1.6 and 20 days (e.g., similar to KOI 377.03 and Kepler-9b). The relative inclination (x-axis) is scaled to show the whole range of relative inclinations from 0 to 90 degrees.

Kepler-9b and 9c, transit timing variations constrain the eccentricities to be $\leq\ 0.2$. Unfortunately, even these modest eccentricities can significantly affect the inferred stellar density.

The challenge of measuring ingress duration and impact parameter and eccentricity is exacerbated by the smearing of the transit light curve in long cadence (LC) data. Due to bandwidth limitations, Kepler sends down data for most of the planetary target integrated over multiple exposures spanning 29.4 minutes (LC). Kepler-9 was observed a LC during Q1-Q3. In future quarters, Kepler-9 will be among a much smaller list of stars observed with short cadence (SC), with an effective integration time of 1 minute. While our measurements of transit times and durations from LC observations are robust, future SC observations will allow for improved measurement of the ingress and egress timescales, impact parameter, orbital inclination and limb darkening model.

Dynamical Phenomenology The striking aspect of the O-C curves of these planets is that they appear to be anti-correlated. First, we fit a parabola to the transit times of each planet

$$\mathrm{C} = \mathcal{A} + \mathcal{B}(t - t_0) + \mathcal{C}(t - t_0)^2 \tag{1}$$

to construct an O-C curve, where t are the transit times, t_0 is the weighted average of the measured t with an inverse variance ($1/\sigma_t^2$) weighting; this choice ensures the $\mathcal{A}$ and $\mathcal{B}$ parameters are uncorrelated; this occurs at BJD 2455088.212, which is our nominal epoch. Now we have several "observed" properties. First, there is $\mathcal{B}_c/\mathcal{B}_b$, which determines the period ratio, which has a best-fitting value of 2.023 currently. Resonant systems have a mean value of this ratio determined by the resonance conditions:

$$2\lambda_c - \lambda_b - \varpi_i = 0, \tag{2}$$

$$2n_c - n_b - d\varpi_i/dt = 0, \tag{3}$$

where here i could be either b or c, λ is the mean longitude, n is the mean motion ($d\lambda/dt$), and ϖ is the longitude of pericenter. So it is clear that the mean value of $2n_c - n_b$ (the difference in the frequency from "exact" resonance) depends on precession ($d\varpi_b/dt$). Given Jupiter-like masses and moderate eccentricities, the long-term average value of P_c/P_b is smaller than 2.023. That means the system, if in resonance, should have a decreasing period ratio at the moment; this is exactly what is observed. A second observed property is the curvature ratio, $-\mathcal{C}_b/\mathcal{C}_c$. Anti-correlation of the parabolas (hence the minus sign) is completely expected, and it is easily reproduced in simulations of 2:1 MMR systems. An energy principle can be used to predict how the curvature ratio is correlated to mass ratio. The Hamiltonian of the two-planet system may be written:

$$\begin{aligned} \mathcal{H} &= \mathcal{H}_b + \mathcal{H}_c + \mathcal{H}_{\rm int} && (4)\\ &\approx -\frac{GM_\star M_b}{2a_b} - \frac{GM_\star M_c}{2a_c}, && (5)\\ & && (6) \end{aligned}$$

where we neglect the potential energy between the two planets ($\sim -GM_bM_c/2r_{bc}$, where r_{bc} is the separation between the planets) because $M_b, M_c \ll M_\star$ whereas $r_{bc} \simeq a_b, a_c$ (there are no close encounters). Then a small amount of energy exchange ΔE from planet c to b, via the gravitational interaction between the planets, leads to semi-major axis changes:

$$\Delta a_b = \frac{2\Delta E}{GM_\star M_b} a_b^2, \quad (7)$$

$$\Delta a_c = \frac{2\Delta E}{GM_\star M_c} a_c^2. \quad (8)$$

Finally, using $\Delta P/P = (3/2)\Delta a/a$, we arrive at:

$$\begin{aligned} -\frac{\Delta P_b/P_b}{\Delta P_c/P_c} = -\frac{\mathcal{C}_b}{\mathcal{C}_c} &= \frac{M_c/a_c}{M_b/a_b} && (9)\\ &\approx (1/2)^{2/3}(M_c/M_b). && (10) \end{aligned}$$

For Kepler-9, the transit timing variations give a value 0.375 for this ratio.

A third observed property is the pattern of points once this parabola is taken away. For a 2:1 resonance, at every transit of the inner body, the outer body will (stroboscopically) be on one side of the star or the other. Therefore, we expect an O-C diagram characterized by "chopping": even and odd transits will be advanced or retarded. These are short-term perturbations of the outer body acting on the inner body, and it is expected that they reveal the mass of the outer body relative to the star. We actually observe this chopping for Kepler-9b, plotted in Figure 1 in the main text. We can make the amplitude of this chopping quantitative by defining the "chop difference":

$$\mathrm{CD} = < \mathrm{O} - \mathrm{C} > |_{\mathrm{even}} - < \mathrm{O} - \mathrm{C} > |_{\mathrm{odd}}. \tag{11}$$

For our data, this is ~ 4 minutes; and integrations easily match that amplitude. The relative phase of the two planets comes into the calculation of the expected amplitude, but fortunately when both planets transit, we know their relative phase. The eccentricities also enter, but they might be partially constrained by light curve analysis and are in any case bounded by stability considerations.

Dynamical Model for Timing Deviations The Newtonian equations of motion in Cartesian coordinates (*21*) are integrated using the suite of numerical integrators in the GNU Scientific Library. It was found experimentally that the Embedded Runge-Kutta Prince-Dormand (8/9 order) was the integrator that reached a chosen precision in the shortest run time, so all integrations used it. We employ astrocentric coordinates within the integration so that the transit geometry, which is with reference to the star, is straightforward. (*22*). A transit mid-time is defined as the time at which the center of the star and planet reach their minimum projected separation. These are found via a Newton-Raphson method. At each transit mid-time, the impact parameter b (in units of AU) and sky-projected velocity v (in units of AU/day) of the transiting planet are

recorded. The transit duration is computed using:

$$D = 2\sqrt{R_\star^2 - b^2}/v, \tag{12}$$

which is roughly the amount of time the center of the planet is on the disk of the star, which is the definition of D from the observations (or the time $(t_3 + t_4)/2 - (t_1 + t_2)/2$, using the standard four points of contact t_i). The integration also outputs the simulated radial velocity of the star at the observation times.

The parameters in the dynamical fit are $[P_j, \lambda_j, e_j \cos\omega_j, e_j \sin\omega_j, i_j]$ – for each planet $j = 0, 1$ – as well as $\Delta\Omega_{\rm sky} \equiv \Omega_c - \Omega_b$, M_b/M_c, M_c, and $R_\star$, where these terms have their standard meanings (*21*). Although the integrations are performed in astrocentric coordinates, we have chosen to fit for orbital parameters in Jacobi coordinates, because they undergo smaller short-term fluctuations (*23*). The epoch is $t - 2454900[BJD] = 188.212$, near the center of the dataset, a choice which ensures the errors on the period and orbital phase of each planet are uncorrelated (*24*).

We used the Levenberg-Marquardt algorithm (*25*) to seek a local minimum for χ^2. This algorithm calls the numerical integrator, computing numerical derivatives of the χ^2 surface by slight adjustment to each input parameter. Typically ~ 20 iterations are required to reach convergence, which is detected via χ^2 changing by less than 10^{-5} in a single iteration. We have included transit mid-times, and a globally-fit impact parameter and duration for each planet, in all dynamical fits. In the final solutions, we also include the radial velocity measurements, in which case we need to introduce an additional free parameter, γ, which allows for the Galactic motion of the star but is irrelevant to the internal dynamics.

Using this method, we found the best-fit constrained by the transit and RV observations in Tables S1, S4, and S5. The simulated transit mid-times and radial velocities of the best-fit are shown in Figure 1 in the main text. We verified that this best-fitting solution is stable for

over 2.7 Gyr using the hybrid integrator of the Mercury package (*26, 27*). Another integration was performed for 2.25 Myr, in which candidate 377.03 was included with its correct period and phase, and a mass of $3.5\ M_{\oplus}$, and it remained stable for the entire integration. The initial conditions corresponding to the best fit solution are given in Table S6.

t_{epoch}	BJD 2455088.212
$M_{\star}$	$1.0 M_{\odot}$ (assumed)
$R_{\star}$	$1.10 \pm 0.09\ R_{\odot}$
M_c	$0.171 \pm 0.013\ M_{Jup}$
M_c/M_b	0.680 ± 0.019
P_b (days)	19.2372 ± 0.0007
$e_b \cos\omega_b$	0.143 ± 0.036
$e_b \sin\omega_b$	0.048 ± 0.008
i_b (degrees)	88.55 ± 0.25
λ_b (degrees)	-9.3 ± 3.2
P_c (days)	38.992 ± 0.005
$e_c \cos\omega_c$	-0.026 ± 0.021
$e_c \sin\omega_c$	0.13 ± 0.04
i_c (degrees)	88.12 ± 0.17
λ_c (degrees)	110.2 ± 2.2

Table S6: Initial conditions corresonding to the best fit solution. These are Jacobi orbital elements. The coordinate system is such that the xy plane is the sky, and z is directed toward the observer. We assume $M_{Jup} = 9.545 \times 10^{-4} M_{\odot}$ and $GM_{\odot} = 2.9591439153 \times 10^{-4} \mathrm{AU}^3/\mathrm{day}^2$. The Jacobi orbital elements are related to the Jacobi Cartesian position and velocity via $M_{\star}+M_b$ for Kepler-9b, and $M_{\star} + M_b + M_c$ for Kepler-9c.

The χ^2 surface as a function of M_c is plotted in Figure 2 in the main text. We plot two curves, one in which the photometry alone is used to constrain the parameters, and one in which the RVs also constrain the planetary mass scale. With the current data, the photometry alone does not constrain the masses of the planets to within two orders of magnitude: they could be anywhere between several Earth masses to several Jupiter masses. This is due to the small number of TTV measurements that have not yet covered a large enough fraction of a resonance libration period; in practice, we found that the eccentricities and inclinations can change significantly to account

for changes in the masses of the planets and resulting in a adequate fit. Therefore radial velocity measurements were scheduled to set the scale of the planets' masses. Per data point, the RVs contribute the most to χ^2, which may mean their uncertainties are underestimated. For our χ^2 calculation transit times and RV measurements are given equal weight; we did not explore regularization of the two different datasets.

Nevertheless, the mass ratio of the planets is given precisely by the relative scale of the transit time deviations, and this quantity (middle panel) is known to within $\approx 2\%$.

We explored whether the planets are truly in resonance with each other by computing critical resonant angles. Within a 3σ range of the best fit, we found some systems have $\theta_1 = \lambda_b - 2\lambda_c - \varpi_b$ librating with full amplitude near 360 degrees, whereas other systems circulated, and many systems switched chaotically between the two. To illustrate this effect, in Figure S3 we present a forward integration of the best-fit system, as well as that of best-fit systems with M_c fixed at 3σ above and below its best value. We conclude we will only be able to address whether the system is in a dynamical resonance once more data have been obtained.

As noted in the main text, we can use the lack of transit duration variations to constrain the mutual inclination of Kepler-9b and 9c (*28, 29*). By fitting for a constant drift in the transit duration in the values in Table S4 and S5, we find $di_b/dt = (2.4 \pm 3.2) \times 10^{-5}$ deg/day and $di_c/dt = (-3 \pm 15) \times 10^{-5}$ deg/day for the respective rates of change of the orbital inclinations for Kepler-9b and 9c. Given the measured masses of Kepler-9b and 9c and assuming secular interactions, we can relate rates of change of inclination to the difference in the longitudes of ascending node of the two planets, $\Delta\Omega_{sky}$ (*29*). We find $\Delta\Omega_{sky} = 2 \pm 3$ deg using Kepler-9b's constraint and $\Delta\Omega_{sky} = 14 \pm 25$ deg using Kepler-9c's constraint. The corresponding $3\,\sigma$ upper limit on the mutual inclination, based on Kepler-9b's constraint, is ~ 10 deg.

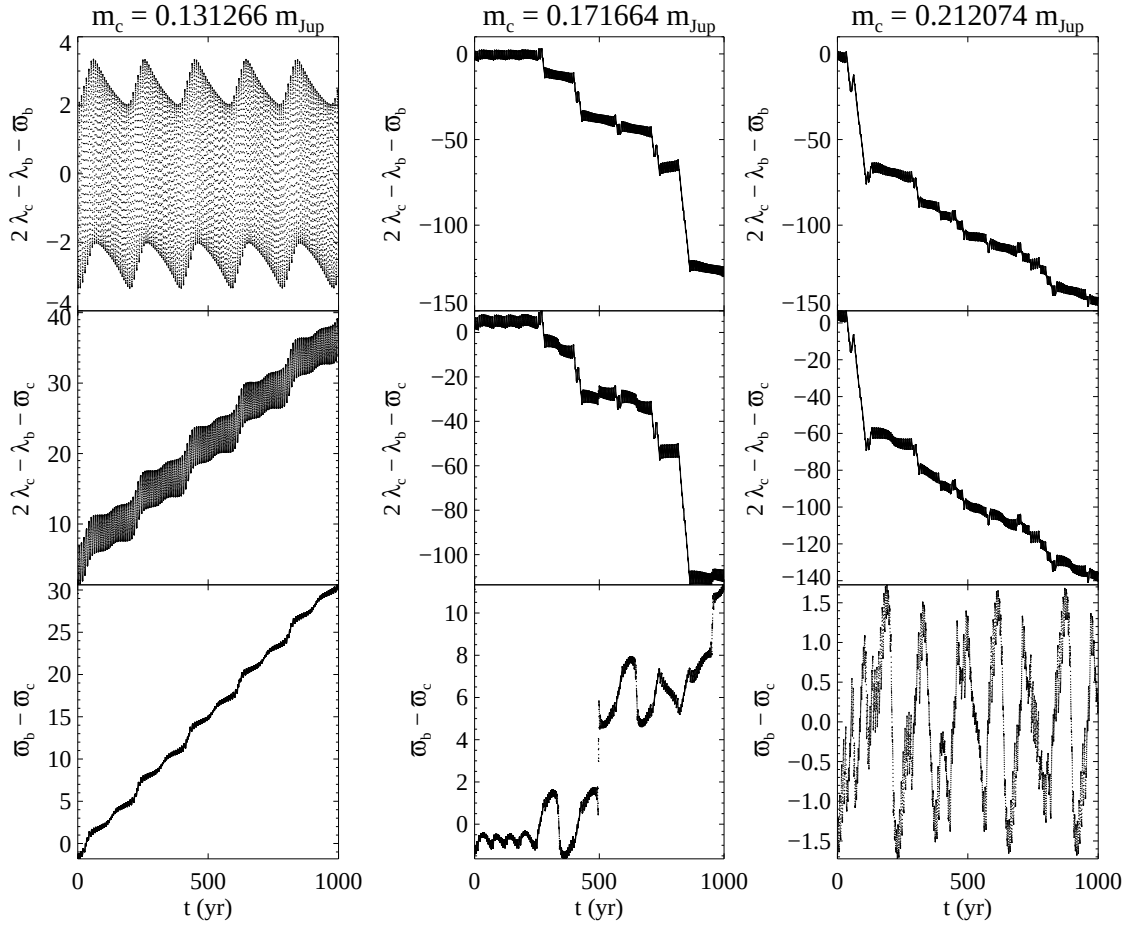

Figure S3: The future resonance angles of three systems, with M_c indicated above the panels and the other parameters chosen to minimize χ^2. Each of these systems is consistent with the current data, yet they display a variety of resonant behaviors over the next millennium. The lower-mass system has its inner planet trapped in an eccentricity resonance, albeit with very large amplitude; the higher-mass system has its two planets participating in a chaotic apsidal resonance.

Dynamical Model for Photometric Observations As further evidence that our solution to the times and durations of transits is viable, we also present in Figure 3 in the main text a full numerical-photometric light curve fit to the Kepler data. This model uses an n-body integrator to calculate the positions of the planets, determines the appropriate light-travel time offsets by correcting the positions to be in the plane of the sky at the distance of the system barycenter, and calculates the sum of the photometric diminutions from both planets using an interpolation on the transiting planet models (*9*). This numerical-photometric model is fully self-consistent (*15*). Figure 3 of the main text shows the light curve of each planet folded and shifted by the transit times listed in Tables S4 and S5. Without this shifting it is obvious by eye that the purely periodic folded photometry does not describe the data well. The model fit from the photometric model and the residuals are also shown, the reduced χ^2 of the fit is $\sim$1.2 for near-transit data, with errors from the scatter of nearby out-of-transit data. The masses and other parameters were taken from the best TTV fits and adjusted slightly. We present the full light curve fit as "proof-of-concept". Though we have not calculated error estimates using this full model, preliminary investigations indicate that the fitting procedure described above accurately describes the limitations of the data in determining the physical and orbital parameters of this system.

Outlook on *Kepler* Monitoring of Kepler-9 We have considered how well the full Kepler data set will improve our solution. If we run our best-fitting solution forward in time, along with the solutions with Mc increased and decreased by 3σ from the best fit value, we find their predicted transit times to diverge by many days (Figure S4), whereas the observed transit times will have uncertainties of $\sim$ 1 minute. Supposing that every transit in the nominal mission (until BJD 2455200) will be observed with the same average precision as we have already achieved, we generated a mock data set based on our current best-fitting solution. Using our L-M minimizer, we resolved the parameters using this "data", and the solution matched the input

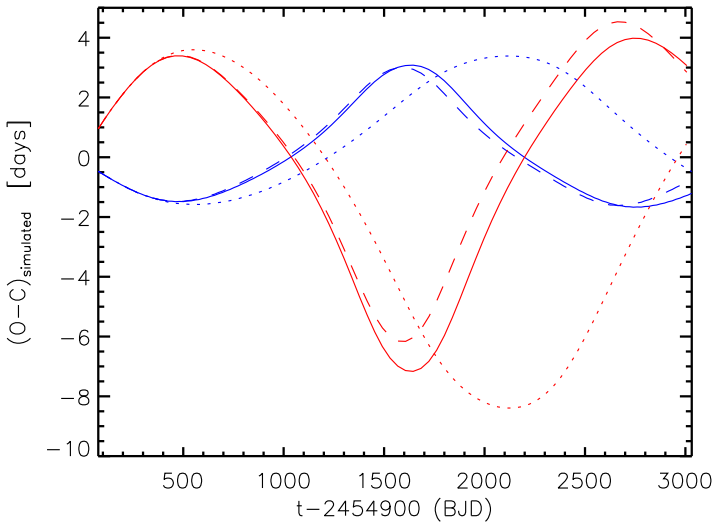

Figure S4: Possible O-C diagrams by the end of the *Kepler* mission. The blue curves correspond to Kepler-9b, and the red curves correspond to Kepler-9c. The solid curves correspond to the best fit solution reported in Table S6. The dotted curves correspond to a fit with M_c fixed at a value $3\ \sigma$ *smaller* than the best fit value. The dashed curves correspond to a fit with M_c fixed at a value $3\ \sigma$ *larger* than the best fit value. The solutions coincide at early times, when the transit times and RV observation constrain the results. The timing deviations are measured in days, where the typical uncertainty in our measured transit times is 10^{-3} days (smaller than the line thickness). The nominal ephemerides to which the numerically integrated transit times are compared have periods of 19.313761 and 38.627078 days, very close to a perfect 2:1 ratio.

to within the reported errors. As the time baseline is extended, the TTV solution will quickly eliminate models that do not fit with the new observations. The mass ratios between the planets and the star will be measured to fractional error $\sim$ 2%, even without input from the already-measured radial velocities. This exercise is a particular example of the general expectation that planetary masses can be measured via transit time variations, independent of radial velocity follow-up (*30*).

References and Notes

1. N. M. Batalha, *et al.*, *Astrophys. J.* **713**, L109 (2010).

2. S. A. Barnes, *Astrophys. J.* **669**, 1167 (2007).

3. S. S. Vogt, *et al.*, *Society of Photo-Optical Instrumentation Engineers (SPIE) Conference Series*, D. L. Crawford & E. R. Craine, ed. (1994), vol. 2198 of *Society of Photo-Optical Instrumentation Engineers (SPIE) Conference Series*, pp. 362.

4. A. W. Howard, *et al.*, *Astrophys. J.* **696**, 75 (2009).

5. J. T. Wright, *Pub. Astron. Soc. Pac.* **117**, 657 (2005).

6. H. T. Isaacson, *Bulletin of the American Astronomical Society* (2009), **41**, 206.

7. P. A. Jansson, *Deconvolution of images and spectra.* (Academic Press, San Diego, CA, 1997).

8. R. L. Kurucz, *et al.*, *National Solar Observatory Atlas* (National Solar Observatory, Sunspot, New Mexico, 1984).

9. K. Mandel, E. Agol, *Astrophys. J.* **580**, L171 (2002).

10. R. L. Gilliland, *et al.*, *Astrophys. J.* **713**, L160 (2010).

11. D. M. Kipping, G. Á. Bakos, *Astrophys. J.*, preprint available at http://arxiv.org/abs/1004.3538.

12. A. Prša, T. Zwitter, *Astrophys. J.* **628**, 426 (2005).

13. F. Castelli, R. L. Kurucz, preprint available at http://arxiv.org/abs/astro-ph/0405087

14. W. H. Press, S. A. Teukolsky, W. T. Vetterling, B. P. Flannery, *Numerical recipes in FORTRAN. The art of scientific computing* (1992).

15. D. Ragozzine, M. J. Holman, *Astrophys. J.*, preprint available at http://arxiv.org/abs/1006.3727.

16. S. Seager, G. Mallén-Ornelas, *Astrophys. J.* **585**, 1038 (2003).

17. A. Sozzetti, *et al.*, *Astrophys. J.* **664**, 1190 (2007).

18. M. J. Holman, *et al.*, *Astrophys. J.* **664**, 1185 (2007).

19. D. M. Kipping, *Mon. Not. R. Astron. S.*, preprint available at http://arxiv.org/abs/1004.3819.

20. K. D. Colón, E. B. Ford, *Astrophys. J.* **703**, 1086 (2009).

21. C. D. Murray, S. F. Dermott, *Solar system dynamics* (Cambridge University Press, 1999).

22. D. C. Fabrycky, *Non-Keplerian Dynamics*, preprint available at http://arxiv.org/abs/1006.3834.

23. M. H. Lee, S. J. Peale, *Astrophys. J.* **592**, 1201 (2003).

24. R. I. Dawson, D. C. Fabrycky, *Astrophys. J.*, preprint available at http://arxiv.org/abs/1005.4050.

25. C. B. Markwardt, *Astronomical Society of the Pacific Conference Series*, D. A. Bohlender, D. Durand, & P. Dowler, ed. (2009), vol. 411 of *Astronomical Society of the Pacific Conference Series*, pp. 251.

26. J. E. Chambers, *Mon. Not. R. Astron. S.* **304**, 793 (1999).

27. J. Wisdom, M. Holman, *Astron. J.* **102**, 1528 (1991).

28. J. Miralda-Escudé, *Astrophys. J.* **564**, 1019 (2002).

29. S. Ballard, *et al.*, *Astrophys. J.* **716**, 1047 (2010).

30. M. J. Holman, N. W. Murray, *Science* **307**, 1288 (2005).